Statistical pitch angle properties of substorm-injected electron clouds and their relation to dawnside energetic electron precipitation

A. Åsnes,[1] R. W. Friedel,[2] J. Stadsnes,[1] M. Thomsen,[2] N. Østgaard,[1] and T. Cayton[2]

Received 11 October 2004; revised 4 January 2005; accepted 10 February 2005; published 14 May 2005.

[1] Using the existing large database of geosynchronous orbit particle measurements from Los Alamos instruments, statistical properties of substorm-injected electron clouds are investigated, with special focus on the pitch angle distribution (PAD) of the electrons. The electron distributions at 6.6 R_E do in general show some anisotropy, and their PADs are probably caused by the combined influence of drift orbits, different for each energy and pitch angle, and pitch angle diffusion due to waves. The statistical results of this paper indicate that the PADs during intervals of increased electron flux at energies greater than 10 keV from midnight till noon are dominated by pitch angle diffusion by interaction with waves. The strength of the pitch angle diffusion is seen to initially limit the growth of anisotropy from differential drift speeds and orbits and later on to increase the anisotropy when the diffusion strength decreases. After local noon we find evidence that pitch angle diffusion is no longer important and the PADs are evolving due to differential drift effects.

Citation: Åsnes, A., R. W. Friedel, J. Stadsnes, M. Thomsen, N. Østgaard, and T. Cayton (2005), Statistical pitch angle properties of substorm-injected electron clouds and their relation to dawnside energetic electron precipitation, *J. Geophys. Res.*, *110*, A05207, doi:10.1029/2004JA010838.

1. Introduction

[2] Particle injections of electrons and protons of energies from a few tens to hundreds of keV [*DeForest and McIlwain*, 1971] in the nightside region are a common feature of substorm expansion onsets and pseudo-onsets. In the dispersionless injection region the flux increase occurs simultaneously in all energies, while outside the dispersionless region the higher-energy particles will arrive first, as they gradient and curvature drift more rapidly than lower-energy particles. For particles of energy lower than ~50 keV the electric convective field becomes important for the drift of the particles, in addition to shifting the spectra in energy as the particles drift across potential lines. This study is focusing on the eastward propagation of the injected electrons, referred to as an electron cloud, and their pitch angle properties as they are measured at geosynchronous orbit.

[3] A phenomenon related to the substorm-injected electron clouds is strong VLF wave activity observed from midnight to the morning local time sector as the cloud of enhanced electron flux drifts eastward. Typically, enhanced whistler mode chorus waves are observed below the electron gyrofrequency [e.g., *Tsurutani and Smith*, 1974; *Meredith et al.*, 2001] and enhanced electrostatic electron cyclotron harmonic (ECH) waves are observed in bands above the electron gyrofrequency [e.g., *Kennel et al.*, 1970]. Among the effects of these waves are pitch angle scattering and resulting electron precipitation from particles scattered into the loss cone.

[4] Chorus waves are generally described to be in the lower and upper band which corresponds to $\omega < 0.5\Omega_{ce}$ and $0.5\Omega_{ce} < \omega < \Omega_{ce}$ [*Inan et al.*, 1992], where ω is the wave frequency and Ω_{ce} is the electron cyclotron frequency. The two bands are observed to be separated by a gap at $\omega = 0.5\Omega_{ce}$. The upper band [*Johnstone et al.*, 1993] and also ECH waves (also mentioned as $(n + \frac{1}{2})\Omega_{ce}$ waves) are considered to be important for the diffuse morningside aurora of lower-energy electron precipitation (down to ~1 keV) [*Inan et al.*, 1992; *Meredith et al.*, 2000; *Horne et al.*, 2003]. Chorus waves at frequencies below half the electron gyrofrequency are considered to be causing the strongly modulated precipitation of >10 keV electrons. The whistler mode chorus waves and ECH waves commonly coexist when observed in regions of electron clouds.

[5] As established by *Kennel and Petschek* [1966], a plasma is unstable to growth of waves when the anisotropy exceeds its critical value. The critical limit of anisotropy is given by equation (1) where the anisotropy parameter A depends on all perpendicular velocities for a given resonant parallel velocity V_R, as given in equation (2). F^{-} is the electron distribution function and $\parallel$ and $\perp$ are directions relative to the background magnetic field

$$A_C = \left(\left| \frac{\Omega_{ce}}{\omega} \right| - 1 \right)^{-1} \quad (1)$$

[1] Department of Physics and Technology, University of Bergen, Bergen, Norway.
[2] Los Alamos National Laboratory, Los Alamos, New Mexico, USA.

0148-0227/05/2004JA010838$09.00

$$A(V_R) = \left. \frac{\int_0^\infty v_\perp dv_\perp \left(v_\parallel \frac{\partial F^-}{\partial v_\perp} - v_\perp \frac{\partial F^-}{\partial v_\parallel} \right) \frac{v_\perp}{v_\parallel}}{2 \int_0^\infty v_\perp dv_\perp F^-} \right|_{v_\parallel = V_R} . \quad (2)$$

This critical anisotropy limit was later tested by *Burton* [1976] and found to be valid using simultaneous wave and particle measurements from Ogo-5. A plasma exceeding the critical flux limit of *Kennel and Petschek* [1966] will be unstable through the loss cone anisotropy. At 6.6 R_E and assuming a lower resonant energy of 30 keV, this critical limit was found to be $\sim 3.5 \times 10^6$ (s sr cm^2)$^{-1}$ [*Baker et al.*, 1981]. The limit of the lower resonant energy is given by equation (3), where ω_{max} is the upper chorus frequency, B is the magnetic field strength, and n_e is the cold plasma density

$$E_{R\parallel} = \frac{B^2}{2\mu_0 n_e} \frac{\Omega_{ce}}{\omega_{max}} \left(1 - \frac{\omega_{max}}{\Omega_{ce}} \right)^3 . \quad (3)$$

[6] Turning equation (1) around gives $\omega_{max} = \Omega_{ce} A/(A+1)$, showing that the higher the anisotropy of the plasma is, the higher the upper frequency of the upper whistler band is allowed to be [*Horne et al.*, 2003]. From equation (3) we notice that this implies that a higher anisotropy will lower the minimum resonant energy for the chorus waves. Equation (3) is only valid for waves propagating parallel to the magnetic field, something which is only nearly true, as wave normal vectors are observed to exist at angles to the background magnetic field up to the resonance cone angle given as $\theta_R = \cos^{-1}(\omega/\Omega_{ce})$ [*Muto et al.*, 1987]. However, the majority of observed waves in the lower band chorus have wave normals within 10° of the background magnetic field [*Goldstein and Tsurutani*, 1984].

[7] In a study with simultaneous observations of chorus waves and electron clouds, *Isenberg et al.* [1982] finds that every electron cloud in the morning sector (out of 18 events) is associated with chorus. Using some assumptions, they also derive lower resonant energies related to the measured waves and find values ranging from 14 to 38 keV.

[8] The precipitation of energetic electrons in the dawn sector related to geomagnetic activity is well known from early experiments by riometers and X-ray detectors on balloons [*Brown*, 1966; *Sletten et al.*, 1971]. With the introduction of global auroral imagers the precipitation related to substorm injections and chorus activity has been seen to extend all the way to the noon sector during quiet periods, with a local maximum in the postdawn sector. During disturbed times the local maximum in precipitation generally occurs in the predawn sector [*Anderson and Chen*, 2002; *Østgaard et al.*, 2000]. The dawn local maximum is not observed in the precipitation of lower energy electrons, indicating that this precipitation consists mainly of energetic electrons [*Østgaard et al.*, 1999].

[9] The effects of a convective field accelerating particles and thus increasing the flux at a given energy as the electrons drift around to the dawnside have been suggested to explain the precipitation in the dawn sector, but this can hardly explain the maximum in the postdawn sector during quiet times where the dawn-dusk convective field should be shifting the spectra to lower energies [*Brice*, 1964]. As indicated by *Kennel and Petschek* [1966] and later shown by *Brice and Lucas* [1971] and *Misra and Singh* [1980], an increase in the cold plasma density would lead to a lowered minimum resonance energy when other parameters were held fixed. As the minimum resonance is lowered, a much larger part of the electrons can resonate with the waves and precipitation will increase. This, together with an observed statistically higher cold plasma density at noon relatively to the nightside [*Higel and Wu*, 1984], is a likely explanation for the postdawn maximum in energetic electron precipitation. An alternative explanation was proposed by *Jentsch* [1976] based on modeling electron drift in a stretched magnetic field model following a nightside injection. His results showed that due to differential longitudinal drift velocities of different pitch angles a sufficient anisotropy to produce wave growth and particle precipitation would occur naturally in the dawn sector.

Table 1. LANL Spacecrafts Used, With Approximate Geographic Longitude and Magnetic Latitude for the Time Period July 2002 to December 2003

Spacecraft	Geographic Longitude	Magnetic Latitude
1990–095	−38	9
1991–080	−165	−1
1994–084	145	−8
LANL-97A	103	−10
LANL-01A	8	2
LANL-02A	69	−8

2. Instrumentation

[10] Geosynchronous orbit has some advantages when it comes to studying the region of dawnside electron precipitation as it passes through the region of strong chorus occurrence and the satellite moves mostly along the electron drift orbits. This makes it acceptable to do a statistical study binning the data only in magnetic local time. The Los Alamos National Laboratory geosynchronous satellites provide multipoint measurements and an extensive database of measurements in the near-Earth plasma sheet at 6.6 R_E. Since 1989, each new satellite has been carrying two instruments, the Magnetospheric Plasma Analyzer (MPA) [*Bame et al.*, 1993; *McComas et al.*, 1993] and the Synchronous Orbit Particle Analyzer (SOPA) [*Belian et al.*, 1992], measuring electron and proton particle flux. MPA measures the energy range from 1 eV to ~47 keV, while SOPA measures >50 keV particles. Together the two instruments cover the energy range of interest regarding substorm injections. The six spacecrafts used in this study are listed in Table 1, together with their geographic longitude and magnetic latitude.

[11] The MPA instrument consists of six telescopes covering the polar angle range of ~25° to ~155°, and with the satellite spin sampled into 24 sectors of 15°, the instrument views ~92% of the unit sphere. For each 15° part of the spin, 40 logarithmically spaced energy channels are sampled and a full electron distribution is obtained in a ~10 s spin. A new sequence of measurements is done every 86 s, making this the practical time resolution of the data set.

[12] As the LANL satellites do not carry magnetometers, a method has been developed [*Thomsen et al.*, 1996, 1999]

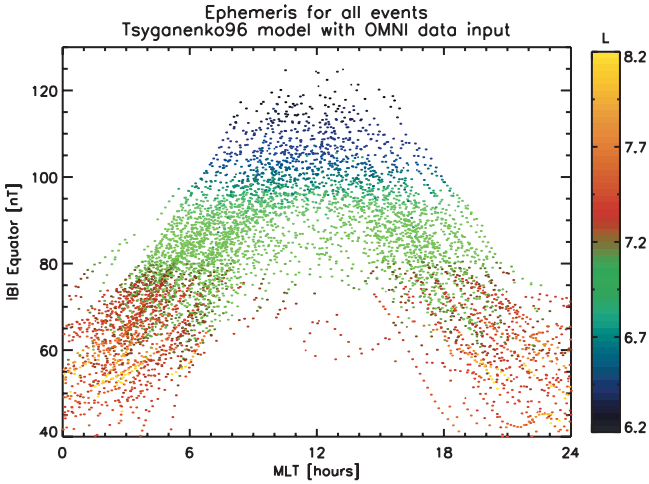

Figure 1. Equatorial *B* field strength mapped from satellite position versus magnetic local time for all events included in study. The color coding indicates the model McIlwain *L* parameter of satellites. The ephemeris parameters are found using the Tsyganenko96 model with input parameters from the OMNI database.

to derive the direction of the magnetic field based on the measured MPA particle distribution. Through moment calculations, a symmetry axis of the temperature is found and, assuming gyrotropy of the particle distribution, this symmetry axis is also the direction of the magnetic field. There is a 180° ambiguity in this field direction, but in the near-Earth region it is safe to assume the field to be northward. Note that as the described method is depending on an anisotropy of the plasma, it will fail when the integrated plasma becomes nearly isotropic, although this does not necessarily mean that the plasma is isotropic at all energies. The strength of the local magnetic field cannot be determined by this method and remains unknown.

[13] The SOPA instrument consists of three telescopes and samples 32 azimuthal sectors per spin. Data is sampled every spin (10 s) but currently the angle resolved data is binned into 10-min intervals. The average magnetic field direction derived from the MPA data over 10-min intervals are used to obtain pitch angle distributions from the SOPA instrument on the same satellite.

[14] As the telescope view angle of MPA is ∼15° and ∼11° for SOPA, the equatorial loss cone which measures ∼2° at geosynchronous orbit cannot be resolved. We should also mention that the LANL satellites carry no wave instrument for chorus detection.

3. Method

[15] The purpose of this paper is to investigate the local properties of the drifting substorm-injected electron clouds at geosynchronous orbit. In order to do this, a statistical study on a large number of injection events has been performed. The events were selected by visually browsing through SOPA spin-averaged data day by day for the period July 2002 to December 2003. To qualify as an injection, the events had to be observed by more than one spacecraft and the event had to show a drift delay between satellites to ensure that the flux increase was not caused by a pressure pulse or other noninjection effects. To avoid overlapping effects of subsequent injections, only fairly isolated injections were selected. An event would only classify as an injection event if a clear flux increase was observed in at least the two lower SOPA energy channels (50–75 keV and 75–105 keV). With these criteria we found 617 observations of injections. However, many of these events did not have the required pitch angle resolved data and were excluded from the study. The events in this study have not been tested to see if there really was a substorm occurring, but we believe that the physical mechanism of particle injections is the same regardless of whether it is a substorm or a pseudo-onset event.

[16] In order to do a superposed epoch study of specific energy channels, it is necessary to remove the difference in dispersion caused by the varying width and local time of the dispersionless injection region. This was done by defining an onset time for each event and for each available energy channel. For each event, only the energy channels that showed a clear flux increase delayed to the increase in higher-energy channels was included in the study. Simultaneous increases in the energy channels were allowed near midnight where dispersionless injections commonly occur.

[17] Using satellite positions and the magnetic field model Tsyganenko96 [*Tsyganenko*, 1995], with input of model parameters from the National Space Science Data Center (NSSDC) near-Earth heliosphere data (OMNI), relevant ephemeris parameters for the events have been obtained. Especially important is the determination of the magnetic local time (MLT) that is used to bin the events, but the McIlwain *L* parameter and the equatorial magnetic field strength mapped along the field line from the satellite position are also important. The latter are shown for all events in Figure 1. The dayside compression and nightside stretching is easily recognizable in this figure, with strong equatorial *B* field and low *L* values at noon compared with high *L* and weak equatorial *B* field at the nightside. It is worth noting that the average equatorial *B* field strength is varying by a factor of two, from 50 nT at midnight to 100 nT at noon. The reason for including the equatorial *B* field here is that it is a parameter in the equation for cyclotron resonant parallel energy (equation (3)).

4. Results

[18] As described in the method section, we split each observation of injected electron clouds into single energy channels and set t_0 to be the time of cloud arrival for each energy. In Figure 2 all events with cloud arrival observed between 0200 and 0400 MLT, normalized by maximum flux in the individual energy channel, are plotted for the top energy channel in MPA (36–47 keV) and the lower channel in SOPA (50–75 keV). MPA data here and in the following have been smoothed over a moving average before normalizing. Note that the satellites move ∼1 hour in magnetic local time per hour so that throughout the time period of the plot the satellite moves ∼3 hours. All the events in Figure 2 show the expected behavior for an injection event, with an initially low flux level followed by a rapid increase at cloud arrival and a slower decay to precloud levels. In this study such a behavior is indeed a selection criterion for the events.

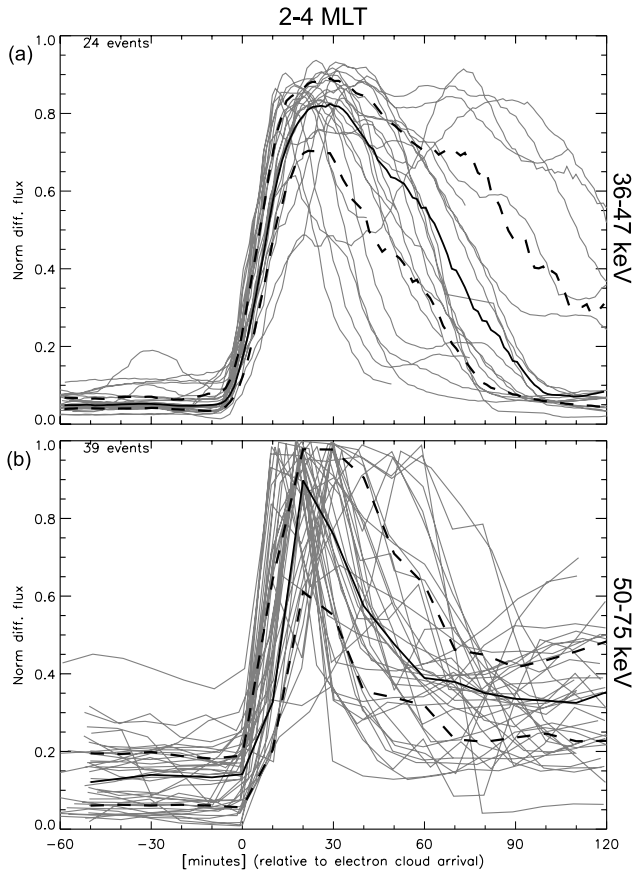

Figure 2. Normalized flux versus time relative to electron cloud arrival at satellite for all events of energy (a) 36–47 keV and (b) 50–75 keV within the sector 0200–0400 MLT. The thick solid and dashed dotted lines indicates median and upper/lower quartiles.

The period of elevated flux for the events varies from 45 min to more extended periods, and the median duration at 0200–0400 MLT and energy 36–47 keV is about 100 min. For lower energies the period of extended fluxes will generally be longer due to the slower azimuthal drift velocity, but in this study the development more than 2 hours after cloud arrival is not plotted. Although the median duration of events found here fits well with the general extension of electron precipitation in a substorm (~2 hours) [*Akasofu*, 1977], these durations may be influenced by the selection criteria we used for the study. Specifically, complex events with more than one injection which also show longer periods of elevated fluxes have been excluded.

[19] Figure 3 shows the median flux values at 36–47 keV from all normalized events for three pitch angles, 90°, 50°, and 20°, for three different local time sectors, 0200–0400, 0600–0800, and 1000–1200 MLT. In these plots an apparent evolution can be seen as the cloud drifts from midnight around to the morningside as the flux increase is gradually becoming less pronounced and drawn out over a longer time period. The extension of the observed cloud at later local times is caused both by the width of the energy bins, as the particles in the top energy range of a bin drift much faster than the particles in the lower energy range, as well as the different drift speeds of different pitch angles. Applying the simple drift model of *Lew* [1961], the difference in drift time for the fastest and slowest electron in the MPA channel 36–46 keV drifting from midnight till noon is ~70 min.

[20] Within the time resolution of the MPA measurements there is no observable delay between the initiation of flux increase at different pitch angles, and as the cloud passes by the satellite the flux levels in the field-aligned electrons appear to follow the flux at perpendicular pitch angles. At

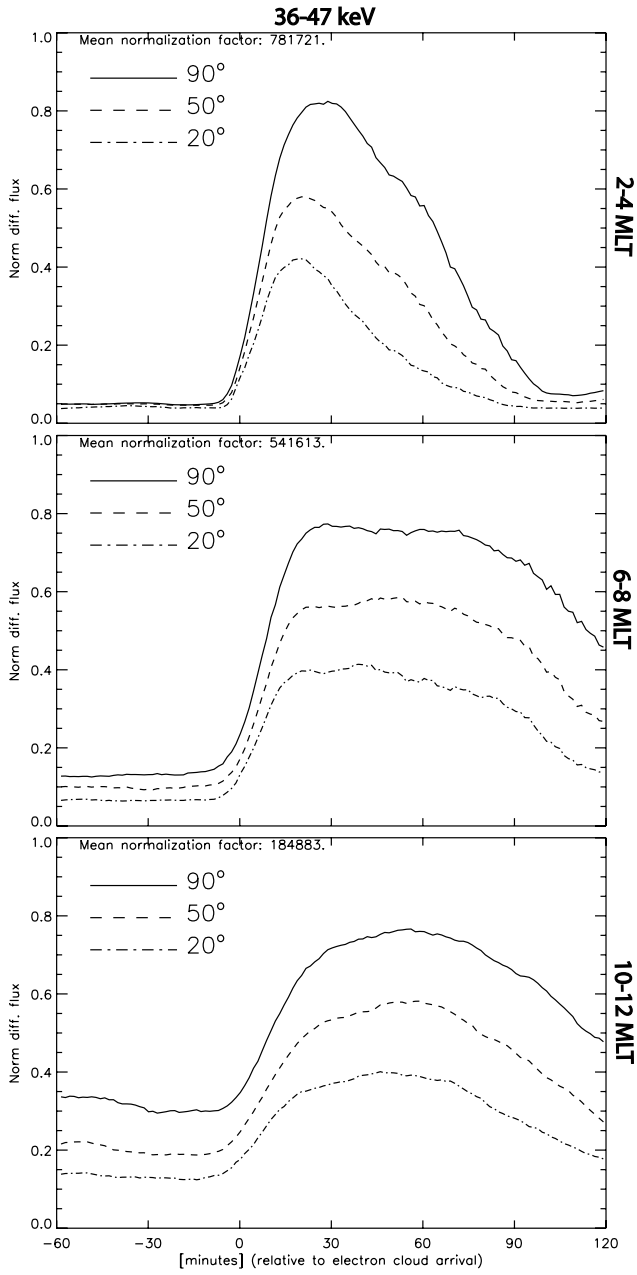

Figure 3. Median normalized flux at 36–47 keV versus time relative to electron cloud arrival at satellite for three pitch angles within the MLT sectors (a) 0200–0400, (b) 0600–0800, and (c) 1000–1200. Pitch angle of 90° is shown by a solid line, 50° is shown by a dashed line, and 20° is shown by a dash-dotted line. Flux at all pitch angles have been normalized by maximum flux at 90°.

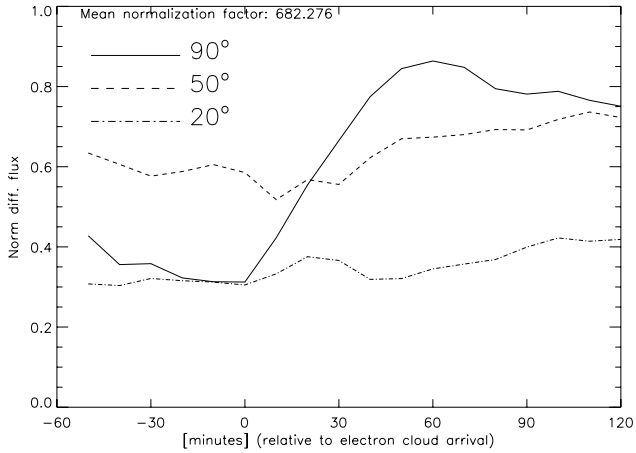

Figure 4. As for Figure 3 but for energy channel 150–225 keV within the sector 0200–0400 MLT.

early local times (Figure 3a) the flux at parallel pitch angles is seen to maximize a few minutes before the maximum at 90° pitch angle. Another feature in these plots is that the growth phase (before cloud arrival) anisotropy changes in local time from a nearly isotropic distribution near midnight to a more anisotropic distribution near noon. As shown in Figure 1, this can be either a result of the satellites moving to lower L shells near noon or a local time effect or both. The behavior of these plots at 36–47 keV is generally reproduced by all MPA energies down to ~10 keV, which was the lowest energy used in this study. However, for the SOPA energy range (>50 keV) the behavior changes as exemplified in Figure 4 for 150–225 keV. Owing to drift shell splitting the nightside shows a field-aligned or butterfly (peaked at intermediate pitch angles, 45° and 135°) pitch angle distribution (PAD) in the growth phase, while after the injection the flux increase is almost entirely at perpendicular pitch angles. The transition energy where the growth phase PADs change from being slightly peaked at perpendicular pitch angles to field-aligned or butterfly [e.g., *Fritz et al.*, 2003] distributions probably indicates a transition from open drift trajectories for lower energies to closed trajectories for the higher-energy particles. The growth phase butterfly or field-aligned distributions are typically observed down to ~50 keV. For electron energies >150 keV there is no observable flux increase in the field-aligned direction in our median results.

[21] In Figure 5 we give an overview of the median maximum fluxes observed at 40° pitch angle in the top MPA energy channel (36–47 keV) for MLT bins running from the injection region around noon to the nightside. Although these values are included mainly to give an overview of the typical flux values, it does indicate that most of the flux loss from the injected electron cloud occurs between midnight and dawn. A steady reduction in the observed maximum flux should be expected from just the differential drift speeds of the range of energies within a bin, but this can only explain some of the flux decrease. If we assume that the changes in flux values from one MLT sector to the next as shown in the inset plot in Figure 5 are caused partly by particles precipitating, the decrease in flux values shows that there are two local maxima in the precipitation, one at midnight which presumably is in the injection region and another in the postdawn region from 0700 to 0900 MLT. This result fits quite well with observations of particle precipitation made by riometers and X-ray detectors born on balloons and satellites [*Hartz*, 1967; *Bjordal et al.*, 1971; *Sletten et al.*, 1971; *Østgaard et al.*, 2000] as well as

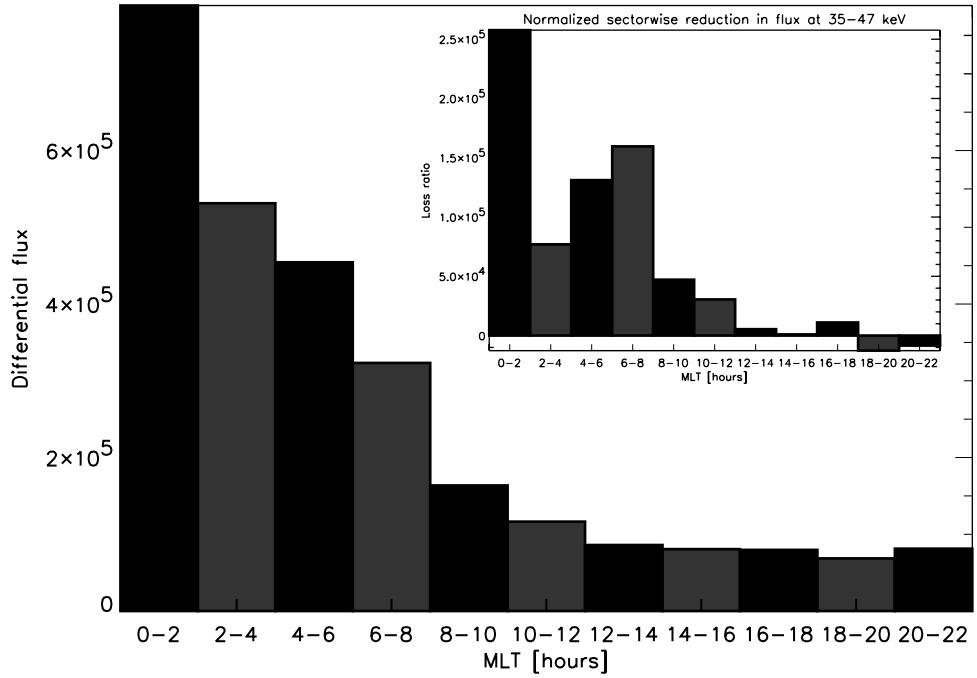

Figure 5. Median maximum flux at 40° in the energy channel 36–47 keV from all events, binned by satellite MLT at time of cloud arrival. The inset figure shows the difference in median flux from one sector to the next.

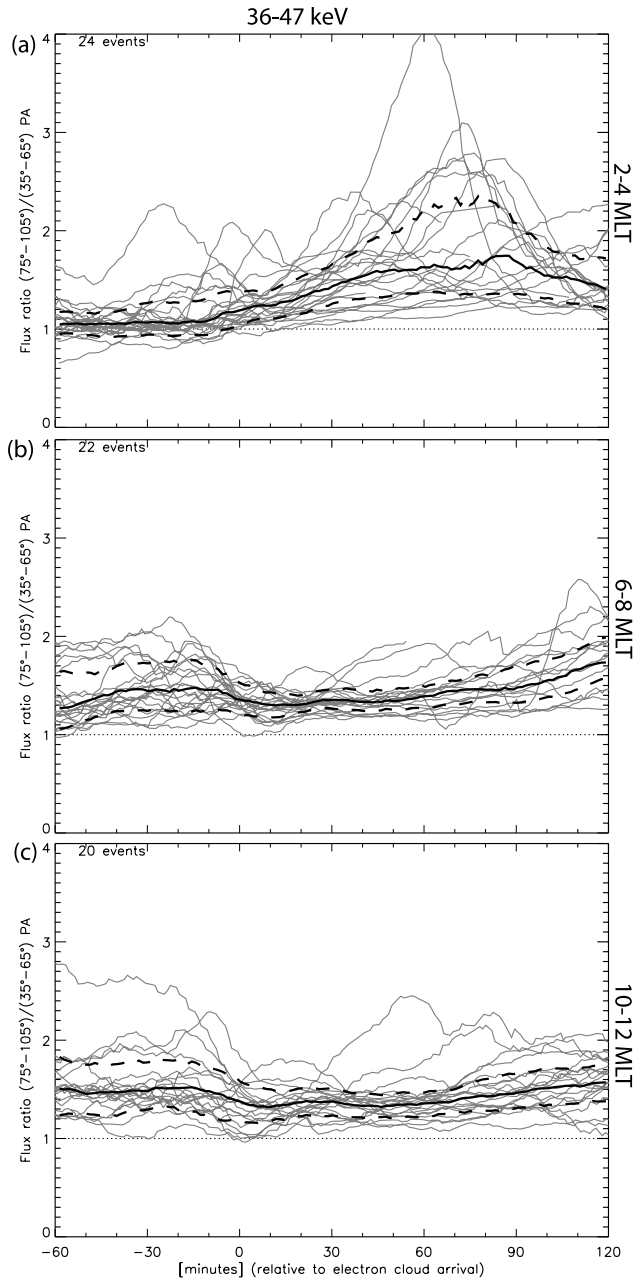

Figure 6. Flux ratio $j(90°)/j(50°)$ versus time relative to cloud arrival at 36–47 keV for each event in MLT bins (a) 0200–0400, (b) 0600–0800, and (c) 1000–1200. Median values are indicated by the thick solid line, while thick dashed dotted lines indicate upper and lower quartiles.

statistical observations of VLF waves [*Parrot and Gaye*, 1994].

[22] In Figure 6 the time development of the flux ratio $j(90°)/j(50°)$ at 36–47 keV is shown for each event in three local time bins, 0200–0400, 0600–0800, and 1000–1200 MLT. T_0 is again set to be the time of cloud arrival at this energy channel. The thick solid line indicates the median value, while the thick dash-dotted lines indicate upper and lower quartile values. In Figure 6a (0200–0400 MLT) the anisotropy is seen to be low initially and later increasing as the cloud arrives at the satellite. At later local times (Figures 6b and 6c) this behavior can be seen to have reversed as the anisotropy is slightly higher in the growth phase than after the cloud arrives. Common for all local times is an increase in the anisotropy some time after the first cloud arrival. This is seen to happen most quickly at early local times, while at 1000–1200 MLT most events do not show a great increase in anisotropy within the time period shown.

[23] The growth of waves from an electron population above the Kennel and Petschek anisotropy limit (equation (1)) is expected to cause some degree of pitch angle diffusion and the strength of diffusion should vary as some function of the measured flux j. As shown by *Roberts* [1969], it is reasonable to assume that the PAD following the injection will decay to a lowest normal mode determined by the local diffusion. In the limit of strong diffusion the diffusion rate is large enough so as to diffuse particles across the loss cone in less than a bounce period [*Lyons*, 1974] and the phase space density distribution will become nearly isotropic over a range of pitch angles where the diffusion is strong. For weak diffusion, particles are slowly scattered into the loss cone, and the slope of the distribution outside the loss cone will be greater than for strong diffusion.

[24] To investigate the degree of anisotropy of the plasma for varying flux levels, the data for all selected events is sorted by MLT bins and energy channels and plotted as flux versus flux ratio of $j(90°)/j(50°)$ for three sectors, 0200–0400 (Figure 7a), 0600–0800 (Figure 7b), and 0800–1000 (Figure 7c) MLT. A striking feature in these figures is that the data appears to be quite well bounded within a triangular frame, at least for the earlier local times. Note that the y axis is logarithmic, so straight lines correspond to exponential functions. The upper side of this limiting triangle, indicated with a solid line (determined visually) in each part of Figure 7 is what can be interpreted as an upper anisotropy limit imposed by the strength of diffusion at a specific flux level. Especially in the earlier MLT sectors, this upper boundary is very well defined, while in later MLT sectors some measurements are outside the limits that confine the majority of the observations. A majority of the observations lie well inside of the upper flux-anisotropy limit.

[25] The lower limit that shows an absence of high anisotropy at low fluxes is also interesting, and it is defined mainly by the plasma observations in the growth phase and trailing edge of the clouds (green and blue points in Figure 7). A third boundary is seen on the left-hand side of each part in Figure 7, setting a lower limit on the anisotropy. This can be interpreted to be an effect of the acceleration mechanism of the energetic plasma (>20 keV) which favors 90° particles [*DeForest and McIlwain*, 1971], most likely because betatron dominates over Fermi acceleration. For the low-energy plasma the injected distribution has been found to be isotropic or field-aligned for the <1 keV electrons [*Moore and Arnoldy*, 1982; *Arnoldy*, 1986].

[26] From the color coding in the scatterplots of flux versus flux ratios a trend can be seen in the plasma behavior as a function of cloud phase. Before cloud arrival the flux is low and the anisotropy is relatively low, although the average anisotropy of the precloud plasma is seen to

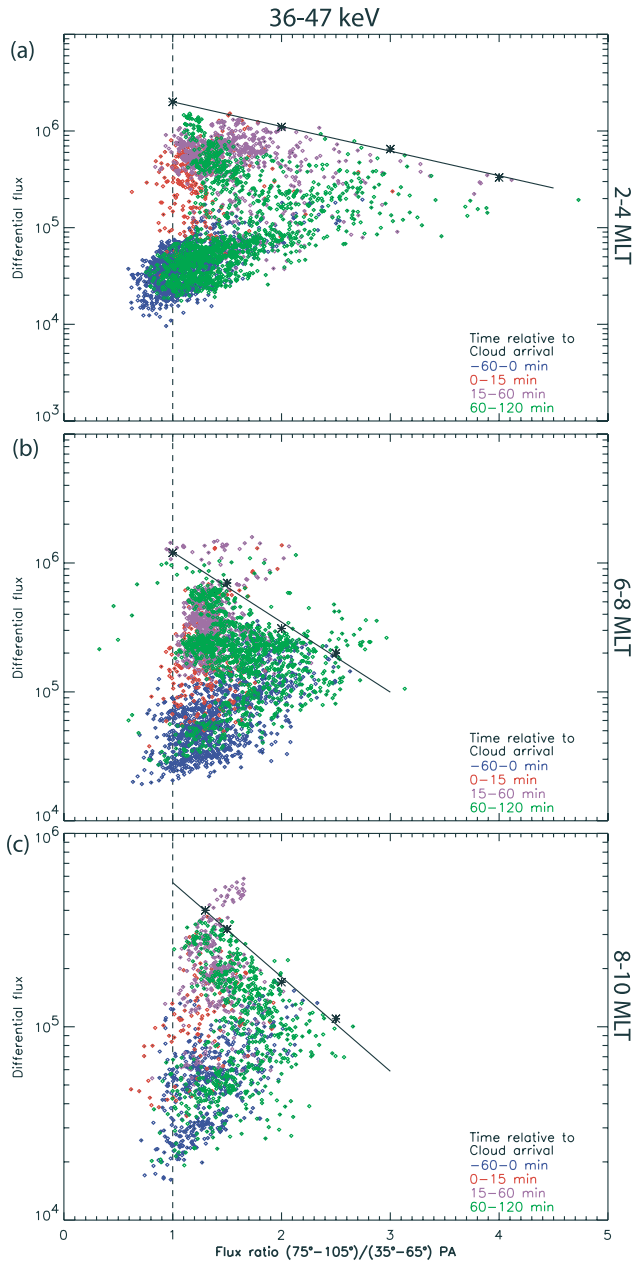

Figure 7. Scatterplot of differential flux versus flux ratio $j(90°)/j(50°)$ at energies 36–47 keV observed when satellite is in the MLT sectors (a) 0200–0400, (b) 0600–0800, and (c) 0800–1000. The colors indicate time relative to cloud arrival, with blue showing 60–0 min before arrival, red showing 0–15 min after arrival, pink showing 15–60 min after, and green showing 60–120 min after cloud arrival.

increase from local night and around the dawnside till noon. The precloud observations (blue) thus make up the lower left corner of the limiting triangle. As the electron cloud reaches the satellite, the flux increases rapidly, while the anisotropy stays relatively low, making up the upper left part of the triangle. The remaining part of the triangle is filled mostly by the trailing part of the electron cloud observed 60–120 min (green) after cloud arrival.

[27] In order to study the time evolution of the flux versus flux ratio in more detail, we show trajectories of flux versus flux ratio at 90°/50° pitch angles for two events in Figures 8–9. Figure 8 shows a trajectory for the energy channel 36–47 keV where the cloud arrives at the satellite at 0427 MLT. The same behavior as suggested by the scatterplots above is seen, where the anisotropy remains low while the flux increases and subsequently increases toward the trailing part of the cloud. When the flux level is approaching the precloud level, the anisotropy suddenly plunges back to the precloud level, completing the cycle. For the second event shown in Figure 9 the observation is made past local noon at 1351 MLT. Here the trajectory also makes a full cycle, but the rotation goes in the anticlockwise direction. These two types of trajectories appear to be typical for dawn and postnoon locations, respectively. It is important to note from comparison with Figure 6 that the change in anisotropy through a cloud is mostly a function of cloud phase and does not depend as much on the satellite movement during the cloud observation. Especially the observation that the initial part of the clouds have more or less the same anisotropy in local times from midnight till noon (∼1.25) proves this.

[28] From Table 2 it is seen that 22 out of 26 events in the sector 0200–0400 MLT for the energy channel 36–47 keV showed a clockwise sense of rotation in flux versus anisotropy (like Figure 8), while the remaining four events did not show any clear rotation. For the SOPA channel 50–75 keV the numbers were 28 events having clockwise rotation, while two made a figure eight trajectory, and for 10 events we were unable to determine a sense of rotation. When doing the same test in the local time sector 1500–1700 MLT, the 36–47 keV channel had four clockwise events, seven anticlockwise events, and three events with a double loop resembling a figure eight trajectory. Three events were unclear. For the channel 50–75 keV at 1500–1700 MLT there were seven clockwise, four anticlockwise, and two figure eights, while eight events were unclear. The implications of this difference in behavior in different local time sectors will be discussed in the following section.

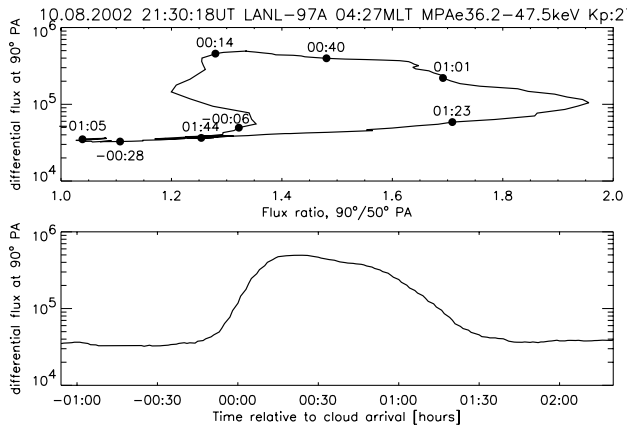

Figure 8. (top) The time trajectory in flux versus flux ratio ($j(90°)/j(50°)$) space for one injected electron cloud observed arriving while spacecraft LANL-97A is at 0427 MLT. (bottom) The corresponding flux ($j(90°)$ pitch angle) versus time relative to cloud arrival. Time labels in upper part corresponds to the times given in bottom part.

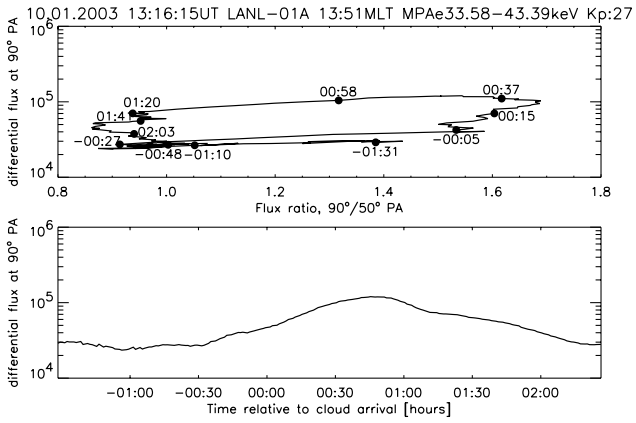

Figure 9. As for Figure 8 but for a different electron cloud, arriving while spacecraft LANL-01A is at 1351 MLT in the postnoon sector.

[29] It should be noticed that the increase in anisotropy toward the end of electron clouds is not simultaneous in all energies. For each energy channel the anisotropy grows when the flux in that specific energy decreases, leading to a dispersion signature in which the energy with high anisotropy decreases with time. This is illustrated in Figure 10, showing a cloud observation made by spacecraft LANL-97A on 24 July 2004. The red band in the anisotropy spectrogram (Figure 10b) starting at the very top energy at 2000 UT and gradually decreasing in energy toward 2400 UT corresponds well to the upper energy of the electron cloud seen in the spectrogram and indicates the high anisotropy trailing part of the cloud. After the red band in the anisotropy spectrogram follows a band of close to isotropic pitch angle distribution seen as interspersed black and yellow corresponding to the very tail of the electron cloud when fluxes are returning to precloud levels. Figure 10c gives the magnetic field elevation in solar magnetospheric (SM) coordinates at the satellite obtained from the plasma distribution through the method described in section 3. A dipolarization occurring with the cloud arrival can be noticed as an increase in the elevation angle starting at 1950 UT.

5. Discussion

[30] In the previous section we have reported some features of nightside injected electron clouds and their pitch angle properties as they drift eastward around dawn. Our goal is to deduce some information on the physical processes affecting these electrons after they have been injected on the nightside. The forces that control the bounce-averaged motion of electrons are the gradient, curvature, and convective E field forces, which affect the different energies and pitch angles at varying degrees. To be able to trace back particles from the satellite to their origin, it would not only be necessary to have a correct magnetic and electric field model, but other influences on the particles would also have to be included. In this paper no attempt will be made at such calculations, but instead simple assumptions based on previous work will be used to interpret the observations of this paper.

[31] The qualitative assumptions used to interpret the time history of the particles observed are the following: (1) At local midnight perpendicular particles curvature/gradient drift faster than field aligned particles while at noon, in a compressed magnetic field, the opposite may be true where perpendicular particles may drift more slowly than parallel particles and intermediate pitch angle particles are the fastest [*Reeves et al.*, 1991]. (2) A dawn-dusk electric field will modify the energies of electrons that gradient and curvature drift across potential lines and also produces significant convective drift of the lower-energy particles. The electron energies are likely to increase in the nightside and decrease on the dayside due to drift orbits crossing potential lines [*Brice*, 1964]. (3) For high-energy particles (>50 keV) the drift orbits are less affected by the convective electric field and drift shell splitting will cause particles at 90° pitch angle to drift closer to the Earth on the nightside and further away on the dayside, while the opposite is true for near field-aligned particles. Particles near 45° PA would circle the Earth more symmetrically, at nearly a constant equatorial crossing distance [*Reeves et al.*, 1991; *Roederer*, 1970].

[32] As for observed pitch angle distributions, two ways are considered for obtaining and maintaining pitch angle anisotropy. One is by differences in drift orbits of different pitch angles and energies. This effect has been modeled by *Jentsch* [1976] in a case relevant to the observations in this paper. Modeling the development of an initially isotropic region of increased flux at midnight in three different magnetic field models, *Jentsch* [1976] found that an anisotropy would naturally develop in the dawn sector, simply from the differential drift velocities as described above. The front of the cloud would have very high anisotropies, with maximum flux at 90° pitch angle, while the trailing part would be field-aligned. At local times near noon, in a dayside compressed magnetic field configuration, the field-aligned particles would drift more quickly and act to reduce the anisotropy at the front of the cloud.

[33] A second process affecting the pitch angle distribution is pitch angle diffusion. In the presence of wave activity the diffusion of particles will always attempt to flatten the phase space density distribution along diffusion curves. The diffusion curves, defining the direction in which electrons can diffuse in interaction with whistler mode chorus waves, are commonly considered to be nearly along curves of constant energy, but for specifically the lower range of resonant parallel energies and when the plasma frequency approaches the electron gyrofrequency, the diffusion curves can deviate significantly from constant energy curves [*Summers et al.*, 1998; *Meredith et al.*, 2002]. In the case of strong pitch angle diffusion extending into the loss cone, the loss cone will be continuously filled, and the

Table 2. Occurrence of Different Types of Flux-Anisotropy Trajectories for Dawn and Postnoon Local Time Electron Clouds

	Number Present at 0200–0400 MLT		Number Present at 1500–1700 MLT	
Trajectory Type	36–47 KeV	50–70 KeV	36–47 KeV	50–75 KeV
Clockwise	22	28	4	7
Anticlockwise	0	0	7	4
Figure eight	0	2	3	2
Undetermined	4	10	3	8
Total	26	40	17	21

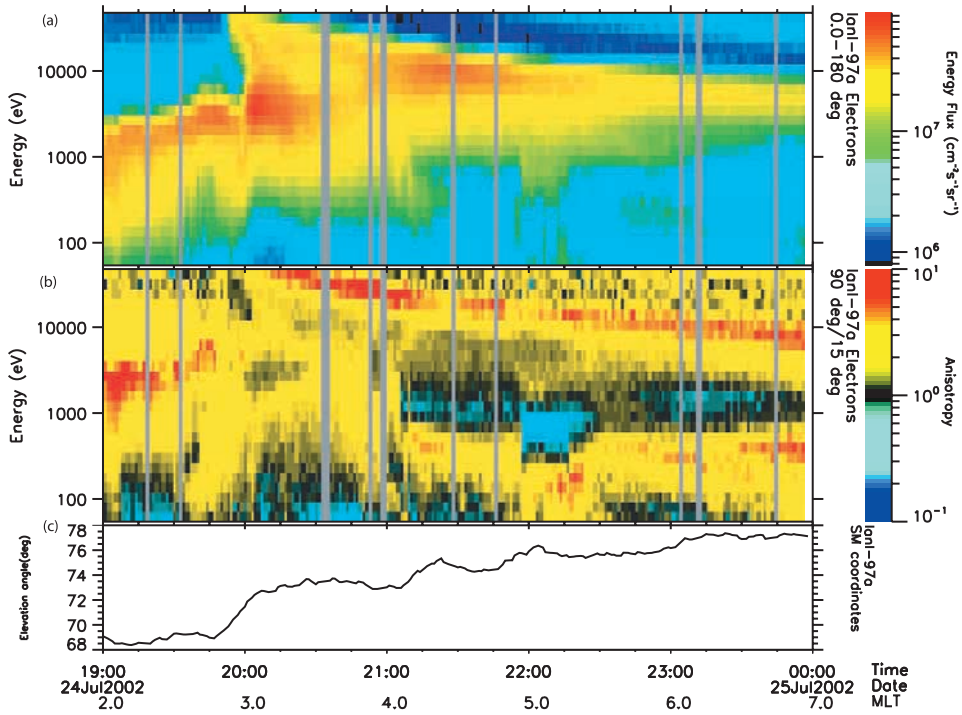

Figure 10. MPA cloud observation by LANL-97A on 24 July 2002. (a) The energy flux spectrogram from 30 eV to 47 keV. (b) A color-coded anisotropy (j(90°)/j(15°)) spectrogram for the same energy range Figure 10a. (c) The magnetic field elevation in SM coordinates. Universal time and MLT calculated with the Tsyganenko 96 model tick marks are shown.

distribution will stay more or less flat along the diffusion curves over the range of pitch angles where the diffusion is strong. In the case of less than strong pitch angle diffusion extending into the loss cone, however, the pitch angle distribution will approach a shape determined by the strength of diffusion. For weak diffusion this will be a gradual slope in the pitch angle distribution down to the loss cone over the range where diffusion dominates, and the slope will become less steep with increasing strength of diffusion. For weak diffusion the time to achieve the natural pitch angle state is expected to be relatively long and may become negligible compared with other effects such as the differences in drift orbits mentioned above.

[34] For pitch angle diffusion originating from wave-particle interactions through the Kennel-Petschek instability, the diffusion strength at different resonant parallel energies will naturally vary, meaning that the pitch angle diffusion at one energy is a function of pitch angle. As there is a minimum resonant energy, this means that there will be no diffusion in a pitch angle range around 90° since particles at these pitch angles have parallel velocities below the resonance limit. At high parallel energies the resonances are of higher order, and their resulting diffusion is weaker than that due to the first-order resonance. As a consequence, the pitch angle diffusion is probably only significant for the observed PADs over a limited energy range. For observations at 6.6 R_E used in this study the loss cone is relatively small (~2°), so the source of free energy is expected to be both in the loss cone and higher pitch angle anisotropy (S. P. Gary, private communication, 2004). Waves produced by anisotropy at high pitch angles at one energy could result in diffusion into the loss cone for a lower energy, while waves growing off the loss-cone anisotropy at one energy would scatter higher pitch angles of higher-energy particles.

[35] The results in this paper are quite opposite of what is expected from only differences in drift orbits as investigated by *Jentsch* [1976], as the most isotropic part of the cloud occurs during high fluxes and high anisotropies are only being observed as the fluxes decrease. Thus the best way to explain the pitch angle observations from the dawn sector is to invoke pitch angle diffusion, initially limiting the growth of anisotropy from the differential drift speeds and orbits of perpendicular and field-aligned particles and later on increasing the anisotropy.

[36] The observations of clockwise and anticlockwise rotation in the flux versus flux ratio space shown in Figures 8–9 also support this conclusion. The clockwise rotation observed in almost every case in the morning sector is a consequence of the anisotropy being limited by pitch angle diffusion which is subsequently decreasing gradually as the fluxes decrease. In the postnoon sector where we sometimes observe anticlockwise rotation the fluxes have already spent some time below the flux limit required for wave growth and subsequent diffusion, and thus the differential drift velocities of particles are allowed to dominate. In this case the anisotropy develops more in line with prediction of *Jentsch* [1976]. Note, however, that in the modeling by *Reeves et al.* [1991] in cases of $K_p = 3$ the field-aligned particles were actually found to drift faster than perpendicular particles for local times a few hours around noon, and in such cases an anticlockwise rotation in flux versus flux ratio space would not be expected.

[37] *Chen and Schulz* [2001] modeled the plasma sheet electrons for storm time conditions, calculating complete

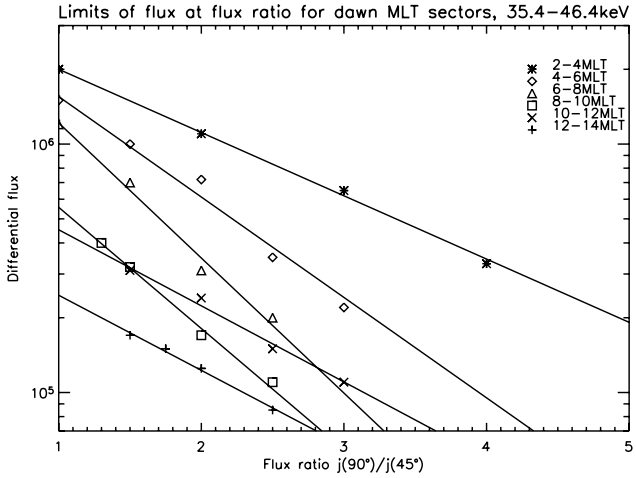

Figure 11. Observed upper flux limits as function of flux ratio $j(90°)/j(50°)$ for a range of MLT bins. The symbols mark points visually obtained from plots shown in Figure 7 and similar plots for MLT bins in between and the solid lines are exponential function fits to these points.

drift orbits in a Dungey model magnetosphere and a cross-tail electric field, including different strengths of pitch angle scattering. In their case of strong diffusion the precipitation was much stronger than observed in the nightside region, while the morning sector hardly saw any precipitation. The observations in this paper supports the conclusion that the pitch angle diffusion is weak for most cases, as we normally see a small anisotropy even at peak fluxes of the electron clouds. Using a model of MLT-dependent pitch angle scattering based on statistical wave observations made by SCATHA's VLF receiver, Chen and Schulz obtained results that were in much better accord with observations of a dawn maximum in the precipitation. However, they did not offer any explanation for why VLF waves are observed most often in the morning sector.

$$E_{R\min\|} = \frac{B^2}{2\mu_0 n_e A(A+1)}. \quad (4)$$

[38] *Hardy et al.* [1990] give the minimum resonant energy for a given magnetic field strength B, electron density n_e, and anisotropy, A, as equation (4). Assuming that the resonance takes place near the geomagnetic equator, we can use the model B field values shown in Figure 1 and the average density values found by *Higel and Wu* [1984] to estimate the impact the variation in these two variables has on the minimum resonant energy. At midnight, a typical density value is 1 electron/cm^{-3} and equatorial magnetic field strength, $|B_{equ}|$ = 50 nT. At 0600 MLT the values are 3 electrons/cm^{-3} and 70 nT, while at noon they are 8 electrons/cm^{-3} and 100 nT. For a given value of the anisotropy one thus finds that the minimum resonant energy at 6 MLT would be a factor 0.65 times the energy at midnight and at noon a factor 0.5. Even with the increase in equatorial B field strength, the minimum resonant energy can be expected to decrease as the electron cloud drifts eastward, in agreement with *Brice and Lucas* [1971]. As reported by *Higel and Wu* [1984], the density can also drop to very low values sometimes, and this may increase the minimum resonant energy by a large enough amount to inhibit wave growth. This could explain the data points seemingly exceeding the upper limit seen in each part in Figure 7.

[39] The effect of the anisotropy on the minimum resonant energy could also be significantly different as a function of local time. From the observations it is seen that the precloud plasma is increasingly more anisotropic from midnight till noon. However, as the injected cloud of a specific energy arrives at the satellite the anisotropy at this energy quickly approaches a typical value of 1.25 in the flux ratio $j(90°)/j(50°)$ (Figure 6), a value that is roughly the same for all MPA energies (<47 keV) until postnoon local times. For higher energies (>100 keV) the anisotropies reach slightly higher values, especially in the noon sector, but the relatively low fluxes at these energies imply that they are not particularly important for the growth of waves and the strength of diffusion. These observations lead us to believe that the local time differences in anisotropy in the electron cloud are not important for explaining the local time distribution of precipitation. However, the relatively high anisotropies at noon in the growth phase plasma may cause the wave growth to start earlier (with only the high-energy particles arrived locally) compared with local times closer to midnight where the anisotropy in this precloud population is less anisotropic. This happens as energy dispersion outside the injection region is causing a mix of growth phase plasma at low energies and cloud plasma at higher energies.

[40] Shown in Figure 11 are the upper flux limits as function of anisotropy observed in the scatterplots in Figure 7 and similar plots for MLT sectors in between. From 0200–0400 MLT and until the sector 0800–1000 MLT the limit is gradually shifted downward while the limits in sector 1000–1400 MLT are slightly higher again, but for these late local times the limit is also difficult to observe. The downward shift of the curves from midnight till 10 MLT indicates that the diffusion and particle precipitation is maintained as the cloud is drifting from midnight till noon even though the flux levels are decreasing and the anisotropy does not change much. We expect the precipitation rate to depend on how quickly this upper flux-anisotropy limit decreases at a given local time.

[41] The most obvious explanation for this observed decrease in the flux-anisotropy limit is that there is a reduction in the minimum resonant energy limit from midnight till noon. Such a reduction would allow an increasingly larger part of the plasma to provide energy to the waves and the critical flux level for wave growth is exceeded even though the flux level at a given energy is decreasing. This means that the use of a fixed flux limit [e.g., *Baker et al.*, 1981] is insufficient for treating different local times or time-varying density and magnetic field.

6. Conclusion

[42] Observations of the pitch angle properties of injected electron clouds have been studied for a range of energies and local times and the differences and similarities have been discussed. It is found that anisotropy of the injected plasma is most likely determined by weak diffusion with a loss cone for fluxes high enough to produce significant wave growth. The flux-anisotropy limit required to grow

waves and produce diffusion is seen to be lowered gradually from midnight till noon, in accordance with the existence of strong dawn precipitation. We believe that this lowering of the flux-anisotropy limit must be caused by a decrease in the magnetic energy per particle from midnight till noon through an increase in the cold plasma density. This will reduce the minimum resonant energy and allow the greater fluxes at lower energies to provide energy to the wave growth. The results in this paper are clearly consistent with earlier observations of precipitation in the dawn sector.

[43] **Acknowledgments.** The authors would like to thank the NSSDC OMNIWeb database for use of OMNI parameters. Funding for A. Åsnes was provided by the Research Council of Norway. The authors appreciate the helpful comments from one of the reviewers.

[44] Lou-Chuang Lee thanks Nigel Meredith and another reviewer for their assistance in evaluating this paper.

References

Akasofu, S.-I. (1977), *Physics of Magnetospheric Substorms*, Springer, New York.

Anderson, P., and M. Chen (2002), Examination of the storm/substorm relationship using global auroral X-ray images, *J. Geophys. Res.*, *107*(A10), 1326, doi:10.1029/2001JA009184.

Arnoldy, R. L. (1986), Fine structure and pitch angle dependence of synchronous orbit electron injections, *J. Geophys. Res.*, *91*(A12), 13,411–13,421.

Baker, D. N., P. Stauning, E. W. Hones Jr., P. R. Higbie, and R. D. Belian (1981), Near-equatorial high-resolution measurements of electron precipitation at L = 6.6, *J. Geophys. Res.*, *86*, 2295–2313.

Bame, S. J., et al. (1993), Magnetospheric plasma analyzer for spacecraft with constrained resources, *Rev. Sci. Instrum.*, *64*, 1026.

Belian, R. D., G. R. Gisler, T. Cayton, and R. Christensen (1992), High-Z energetic particles at geosynchronous orbit during the great solar proton event series of October 1989, *J. Geophys. Res.*, *97*, 16,897–16,906.

Bjordal, J., H. Trefall, S. Ullaland, A. Bewersdorff, J. Kangas, P. Tanskanen, G. Kremser, K. H. Saeger, and H. Specht (1971), On the morphology of auroral-zone X-ray events - 1. Dynamics of midnight events, *J. Atmos. Terr. Phys.*, *33*, 605–626.

Brice, N. (1964), A qualitative explanation of the diurnal variation of chorus, *J. Geophys. Res.*, *69*, 4701.

Brice, N., and C. Lucas (1971), Influence of magnetospheric convection and polar wind on loss of electrons from the outer radiation belt, *J. Geophys. Res.*, *76*(4), 900–908.

Brown, R. R. (1966), Electron precipitation in the auroral zone, *Space Sci. Rev.*, *5*, 311–387.

Burton, R. K. (1976), Critical electron pitch angle anisotropy necessary for chorus generation, *J. Geophys. Res.*, *81*(25), 4779–4781.

Chen, M. W., and M. Schulz (2001), Simulations of diffuse aurora with plasma sheet electrons in pitch angle diffusion less than everywhere strong, *J. Geophys. Res.*, *106*(A12), 28,949–28,966.

DeForest, S. E., and C. E. McIlwain (1971), Plasma clouds in the magnetosphere, *J. Geophys. Res.*, *76*, 3587.

Fritz, T. A., M. Alothman, J. Bhattacharjya, D. L. Mathews, and J. Chen (2003), Butterfly pitch-angle distributions observed by ISEE-1, *Planet. Space Sci.*, *51*(3), 205–219.

Goldstein, B. E., and B. T. Tsurutani (1984), Wave normal direction of chorus near the equatorial source region, *J. Geophys. Res.*, *89*(A5), 2789–2810.

Hardy, D. A., W. J. Burke, and E. Villalon (1990), Electron dispersion events in the morningside auroral zone and their relationship with VLF emissions, *J. Geophys. Res.*, *95*(A5), 6451–6466.

Hartz, T. R. (1967), The general pattern of auroral particle precipitation, *Planet. Space Sci.*, *15*, 301–329.

Higel, B., and L. Wu (1984), Electron density and plasmapause characteristics at 6.6 R_E: A statistical study of the GEOS 2 relaxation sounder data, *J. Geophys. Res.*, *89*, 1583.

Horne, R. B., R. M. Thorne, N. P. Meredith, and R. R. Anderson (2003), Diffuse auroral electron scattering by electron cyclotron harmonic and whistler mode waves during an isolated substorm, *J. Geophys. Res.*, *108*(A7), 1290, doi:10.1029/2002JA009736.

Inan, U. S., Y. T. Chiu, and G. T. Davidson (1992), Whistler-mode chorus and morningside aurorae, *Geophys. Res. Lett.*, *19*(7), 653–656.

Isenberg, P. A., H. Koons, and J. Fennel (1982), Simultaneous observations of energetic electrons and dawnside chorus in geosynchronous orbit, *J. Geophys. Res.*, *87*, 1495–1503.

Jentsch, V. (1976), Electron precipitation in the morning sector of the auroral zone, *J. Geophys. Res.*, *81*, 135–146.

Johnstone, A. D., D. M. Walton, R. Liu, and D. A. Hardy (1993), Pitch angle diffusion of low-energy electrons by whistler mode waves, *J. Geophys. Res.*, *98*, 5959–5967.

Kennel, C. F., and H. E. Petschek (1966), Limit on stably trapped particle fluxes, *J. Geophys. Res.*, *71*, 1–28.

Kennel, C. F., F. L. Scarf, R. W. Fredricks, J. H. McGhee, and F. V. Coroniti (1970), VLF electric field observations in the inner magnetosphere, *J. Geophys. Res.*, *75*, 6136.

Lew, J. A. (1961), Drift rate in a dipole field, *J. Geophys. Res.*, *66*, 2681–2685.

Lyons, L. R. (1974), Electron diffusion driven by magnetospheric electrostatic waves, *J. Geophys. Res.*, *79*, 575.

McComas, D. J., et al. (1993), Magnetospheric plasma analyzer: Initial three-spacecraft observations from geosynchronous orbit, *J. Geophys. Res.*, *98*, 13,453.

Meredith, N. P., R. B. Horne, A. D. Johnstone, and R. R. Anderson (2000), The temporal evolution of electron distributions and associated wave activity following substorm injections in the inner magnetosphere, *J. Geophys. Res.*, *105*(A6), 12,907–12,917.

Meredith, N. P., R. B. Horne, and R. R. Anderson (2001), Substorm dependence of chorus amplitudes: Implications for the acceleration of electrons to relativistic energies, *J. Geophys. Res.*, *106*(A7), 13,165–13,178.

Meredith, N. P., R. B. Horne, D. Summers, R. M. Thorne, R. H. A. Iles, D. Heynderickx, and R. R. Anderson (2002), Evidence for acceleration of outer zone electrons to relativistic energies by whistler mode chorus, *Ann. Geophys.*, *20*, 967.

Misra, K. D., and B. D. Singh (1980), On the modifications of the whistler mode instability in the magnetosphere in the presence of parallel electric field by cold plasma injection, *J. Geophys. Res.*, *85*, 5138–5142.

Moore, T. E., and R. L. Arnoldy (1982), Plasma pitch angle distribution near the substorm imjection front, *J. Geophys. Res.*, *87*(A1), 265–270.

Muto, H., M. Hayakawa, M. Parrot, and F. Lefeuvre (1987), Direction finding of half-gyrofrequency VLF emissions in the off-equatorial region of the magnetosphere and their generation and propagation, *J. Geophys. Res.*, *92*(A7), 7538–7550.

Østgaard, N., J. Stadsnes, J. Bjordal, R. R. Vondrak, S. A. Cummer, D. Chenette, G. K. Parks, M. J. Brittnacher, and D. L. McKenzie (1999), Global scale electron precipitation features seen in UV and X rays during substorms, *J. Geophys. Res.*, *104*, 10,191–10,204.

Østgaard, N., J. Stadsnes, J. Bjordal, R. R. Vondrak, S. A. Cummer, D. L. Chenette, M. Schulz, and J. G. Pronko (2000), Cause of the localized maximum of X-ray emission in the morning sector: A comparison with electron measurements, *J. Geophys. Res.*, *105*(A9), 20,869–20,884.

Parrot, M., and C. A. Gaye (1994), A statistical survey of ELF waves in a geostationary orbit, *Geophys. Res. Lett.*, *21*, 2463–2466.

Reeves, G. D., R. D. Belian, and T. A. Fritz (1991), Numerical tracing of energetic particle drifts in a model magnetosphere, *J. Geophys. Res.*, *96*(A8), 13,997–14,008.

Roberts, C. S. (1969), Pitch angle diffusion of electrons in the magnetosphere, *Rev. Geophys.*, *7*, 305.

Roederer, J. G. (1970), *Dynamics of Geomagnetically Trapped Radiation*, Springer, New York.

Sletten, A., J. Stadsnes, and H. Trefall (1971), Auroral-zone X-ray events and their relation to polar magnetic substorms, *J. Atmos. Terr. Phys.*, *33*, 589–604.

Summers, D., R. M. Thorne, and F. Xiao (1998), Relativistic theory of wave-particle resonant diffusion with application to electron acceleration in the magnetosphere, *J. Geophys. Res.*, *103*, 20,487–20,500.

Thomsen, M. F., D. J. McComas, G. D. Reeves, and L. A. Weiss (1996), An observational test of the Tsyganenko (T98) model of the magnetospheric field, *J. Geophys. Res.*, *101*(A11), 24,827–24,836.

Thomsen, M. F., E. Noveroske, J. E. Borovsky, and D. J. McComas (1999), Calculation of moments from measurements by the Los Alamos magnetospheric plasma analyzer, *Tech. Rep. LA-13566-MS*, Los Alamos Natl. Lab., Los Alamos, N. M.

Tsurutani, B. T., and E. J. Smith (1974), Postmidnight chorus: A substorm phenomenon, *J. Geophys. Res.*, *79*, 118.

Tsyganenko, N. A. (1995), Modelling the earth's magnetospheric magnetic field confined within a realistic magnetopause, *J. Geophys. Res.*, *100*, 5599.

A. Åsnes, N. Østgaard, and J. Stadsnes, Department of Physics and Technology, University of Bergen, Allegt. 55, 5007 Bergen, Norway. (arne.asnes@ift.uib.no; nikost@ift.uib.no; johan.stadsnes@ift.uib.no)

T. E. Cayton, R. H. W. Friedel, and M. Thomsen, Los Alamos National Laboratory, P.O. Box 1663, Los Alamos, NM 87545, USA. (tcayton@lanl.gov; friedel@lanl.gov; mthomsen@lanl.gov)